Characteristics of turbulent boundary layer large scale motions using direct fluctuating wall shear stress measurements

Rommel J. Pabon,* Lawrence Ukeiley, and Mark Sheplak
University of Florida, Gainesville, Florida 32611, USA

Casey Barnard Keane
Sandia National Laboratories, Albuquerque, New Mexico 87123, USA

(Received 14 June 2018; published 8 November 2018)

This experimental work studies the impact large scale motions in a zero pressure gradient turbulent boundary layer have on the fluctuating streamwise wall shear stress component using a recently developed $1 \times 1\,\mathrm{mm}^2$ floating element differential capacitive shear stress sensor. The sensing system allows for a flat band response with a bandwidth up to 1.8 kHz (based on a $\pm$3-dB limit). The streamwise velocity is measured using single component hot-wire anemometry. The experimental setup is first verified to have a canonical zero pressure gradient turbulent boundary layer using the mean and fluctuating velocity profiles as well as fits for the mean wall shear stress with respect to the operating Reynolds number. Characteristics of the large scale structure are examined spatially using Taylor's frozen field hypothesis and the lag time of peak levels of correlation between the shear stress and velocity signals. The large scale motion inclination angle is determined to be 16°. The coherence between the signals demonstrate that low frequency motions dominate most of the boundary layer except nearest the wall. In addition, conditional sampling of velocity on shear stress provides conditional velocity statistics profiles which reveal information on the entire boundary layer during shear stress events, representing the qualitative features of the bursting-sweeping process.

DOI: 10.1103/PhysRevFluids.3.114604

I. INTRODUCTION

For the multitude of engineering problems involved with fluid flowing relative to a body, the knowledge of wall shear stress τ_w over the body can elucidate much more than just the viscous drag. Locations of separation, cavitation, and transition to turbulence, as well as local flow direction, and heat transfer rate can be described in some part through accurate wall shear stress measurement. For turbulent boundary layers, the mean wall shear stress $\overline{\tau_w}$, along with the fluid density ρ, also describe the friction velocity $u_\tau = \sqrt{\tau_w/\rho}$. This is an important scaling parameter for physics occurring very close to the wall where viscous forces become as important as inertial forces. The fluctuating component of wall shear stress $\tau_w' = \tau_w - \overline{\tau}_w$, along with the fluctuating pressure, describes a more comprehensive picture of the effect turbulent motions have on the surface. This knowledge can lead to more targeted flow control apparatus for practical situations such as drag reduction, delaying stall, or localized cooling. However, direct experimental and numerical measurements of τ_w' have, until recently, suffered from a lack of spatial and temporal resolution to resolve these turbulent motions.

*rjpabon91@ufl.edu

 ©2018 American Physical Society

Relevant reviews of wall shear stress measurement techniques were given by Winter [1], which focused on mean measurements, Haritonidis [2], which introduced the concept of micromachined shear sensors, and Naughton and Sheplak [3], which suggested that the current manufacturing technology has allowed direct sensing methods to be achievable for measuring the fluctuating shear stress, particularly with the use of miniature floating element–type sensors. Previous studies have used thermal anemometry, at the wall, for shear stress measurement, available commercially as sublayer hot-film probes, but they suffer from various issues, particularly frequency-dependent conduction effects. This has resulted in the wide range of values for the relative fluctuating wall shear stress intensity $\tau'^{+}_{w,rms} = \tau'_{w,rms}/\overline{\tau}_w$ in canonical turbulent boundary layers that the literature has provided, ranging from 0.06 to 0.45, collected in a review by Wietrzak and Lueptow [4]. In numerical simulations, values for $\tau'^{+}_{w,rms}$ and even averaged shear relations like the skin friction coefficient $c_f = 2\overline{\tau}_w/\rho U_\infty^2 = 2(U_\infty^+)^{-2}$ in the turbulent regime show discrepancies, due to spatial development of the simulation and sensitivity to the simulation's conditions, e.g., inflow boundary conditions and resolution. Until these recent simulations by Schlatter and Örlü [5], which show $\tau'^{+}_{w,rms}$ proportional to the logarithm of the Reynolds number up to the $O(10^3)$, the accepted value was believed to asymptote in the turbulent regime to 0.4 by the seminal work of Alfredsson *et al.* [6]. The micropillar method of Brücker *et al.* [7], an optical technique based on deflection of small pillars, is able to reconstruct a spatiotemporal field of the wall shear stress on the wall [8]; however, this indirect method still requires strict assumptions on the flow, such as the linearity of the viscous sublayer (in an instantaneous sense), and no significant energy in the resonance for accurate measurements. A recent technique involving microelectromechanical system (MEMS) based manufacturing is the elastic film based sensor of Amili and Soria [9], which is not intrusive like the micropillar method and uses direct shear stress-strain relationships to transduce displacement monitored by optical techniques. This technique shows promise, especially in its ability to capture the spatial shear stress field and scale well with increasing loading to much larger shear values, but bandwidth up to 240 Hz limits applicable Reynolds numbers. Ultimately for the current study, repeatable and accurate wall shear stress measurements are necessary to verify the footprint of coherent structures on the wall shear stress.

The turbulent boundary layer has been observed to have organized structure to a certain degree; these recurring patterns must exhibit significant levels of correlation of flow properties for a substantial spatiotemporal extent. While difficult to exactly define for all cases, coherent structures provide a framework to view the energy and momentum transfer in a flow as a superposition and interaction of motions at least larger than the dissipation scales. The characterization of coherent structures in a turbulent boundary layer has revealed the importance of scale separation, with streaks, quasistreamwise and hairpin vortices populating the inner layer, and large scale motions (LSMs) as well as very large scale motions (VLSMs) that are theorized to originate from organization of the smaller scales [10,11]. The increased wall shear stress intensity in high frequencies during passage of LSMs associated with the bursting process further suggests the interplay between motions of vastly different scales [12]. This has been characterized more concretely in the recent confirmation that the small scale motions near the wall are modulated by the outer layer and large scale component, especially at higher Reynolds numbers [13].

Using the matching layer between this inner region and the outer layer and assuming the logarithmic profile matches asymptotically in both regions results in the Coles-Fernholz relation for the skin friction coefficient $c_f = 2(\kappa^{-1}\,\mathrm{Re}_\theta + C)^{-2}$ [14]. High Reynolds number experiments have reported the constants for the mean velocity profile $U^+ = \kappa^{-1}\ln y^+ + B$ as $\kappa = 0.384$, $B = 4.17$ [15,16], and $C = 4.127$ [17]. As accurate measurements have been possible at ever increasing Reynolds number, questions continue to arise on the veracity of long suggested trends such as the universality of the logarithmic layer in the overlap region [18], the origin and evolution of these large scale structures as resulting from organized smaller scales [19], and the k^{-1} energy spectrum, expected when more scales begin to overlap with increased energy input [20,21]. The increasing realization that quality high Reynolds number experiments in canonical turbulent boundary layers are producing unexpected results indicates that experimental methods in tandem with new sensing

techniques and simulation verification are the way to understand the increasing effect these LSMs and VLSMs are having on the wall.

The goal of the present study is to further develop the understanding of the dynamics of wall shear stress, specifically from the large scales that have a significant impact in momentum transfer as Reynolds number increases. The primary method used to extract this impact is an independent direct time resolved measure of wall shear stress sampled synchronously with the streamwise velocity above. With that aim and design in mind, the transduction scheme chosen was a MEMS based floating element–type capacitive shear stress sensing system that can capture spatially and temporally resolved skin friction measurements. This is a direct transduction scheme that does not rely on restrictive assumptions about the flow in contrast to thermal anemometry, the Clauser chart method, or sublayer structures like micropillars. Current fabrication methods allow for negligible misalignment errors and limited flow disturbances. A low-pass filter alleviates the sensor response near resonance without affecting the frequencies in the flat band region. With a point skin friction sensor, the conditional friction velocity can be extracted based on a desired condition that best represents a particular structure. This sensor is thus suited for testing future conditional eddy models of wall shear stress.

II. EXPERIMENTAL METHODS

A. Experimental facility

An Engineering Laboratory Design (ELD) 407B closed-circuit wind tunnel at the University of Florida was used to conduct the experiments in this investigation. The ELD tunnel has a square test section of $0.61 \times 0.61\,\mathrm{m}^2$ cross section that is 2.44 m long, with sidewalls and floors all composed of 19.1-mm-thick clear acrylic, allowing optical access to the tunnel without significant optical distortion. A variable frequency drive outputs a constant frequency power signal to control an in-line three phase 440 V and 200 HP electric motor which itself drives a two stage axial fan, which allows for a velocity range up to $90\,\mathrm{ms}^{-1}$.

Downstream of the fan and first set of turning vanes, an in-line heat exchanger is installed with an external chiller unit supplying water as the coolant fluid at 13 °C. Coolant supply to the heat exchanger is regulated by a modulating valve actuator using a temperature set point controller with the thermocouple downstream of the exchanger. The cooling system is able to sustain a set temperature within ± 1 °C. Thus, using a constant air temperature assumption, other thermodynamic properties such as density and viscosity are assumed constant, using interpolated values and the average run temperature. Downstream of this heat exchanger and the second set of turning vanes is the main flow conditioning section, consisting of a honeycomb section and graduated mesh and porosity screens to reduce turbulence levels entering the test section. Downstream of this section is the 25:4 area contraction and then the test section. Measured freestream turbulence intensity levels are below 0.15% as measured by the hot-wire anemometer at the streamwise location of the shear sensor, centered in the spanwise direction, and far from the test section walls and flat plate model in the wall-normal direction. This is a more conservative approach and will result in higher turbulence intensity levels than measurements at the inlet plane of the test section.

A traversing ceiling is installed into the test section capable of three degrees of freedom linear translation from Velmex Unislide components driven by dc stepper motors, with the screw drives controlled by a Velmex VXM controller. This traversing system is utilized to position the hot-wire probe as desired with respect to the capacitive shear stress sensor (CSSS). The minimum step size of the traverse system is 6.35 μm in the wall-normal and streamwise directions and 12.7 μm in the spanwise direction. For the typical run speed in the study, $20\,\mathrm{ms}^{-1}$, this corresponds to a minimum step size of 0.32 and 0.64 viscous units, respectively. A supporting arm attached to the screw drive is used to mount the desired probe, which, in this study, is a hot-wire anemometer. A three-dimensional printed plastic NACA0012 airfoil profile surrounds the supporting arm to prevent shedding-induced vibrations as well as support the instrumentation wiring.

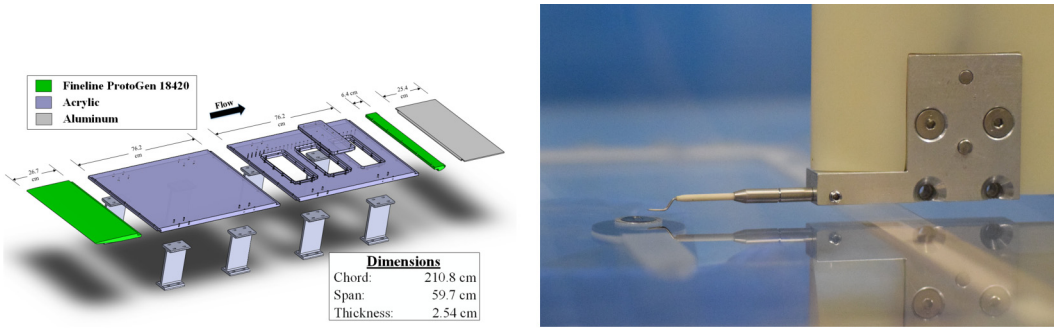

(a) (b)

FIG. 1. (a) Schematic of the flat plate model and supports (coloring for clarity) and (b) flat plate model installed with hot-wire mount descending from the traversing ceiling with capacitive shear stress sensor in view.

B. Flat plate model

Figure 1(a) shows a schematic of the flat plate model used in this study to create a zero pressure gradient turbulent boundary layer, which is installed in the test section of the ELD wind tunnel. The green colored pieces (false color) are stereolithography printed with a plastic approximating acrylonitrile butadiene styrene properties. The leading edge profile was chosen from the optimization study of Hanson *et al.* [22], which sought to create a profile that led to the minimum length of the nonzero pressure gradient region on the top surface. The trailing edge piece also consists of a hinge to allow rotation of the aluminum trailing edge piece and can be placed at a desired angle by tightening the hinge, along with additional rods to support the weight of the aluminum trailing edge piece, installed from the tunnel floor. The aluminum supports under the model are mounted to the tunnel and the model itself, with rubber panels between the supports, model, and the tunnel floor to reduce the effect of tunnel vibrations affecting measurements. A photograph of the installation is shown in Fig. 1(b), along with the hot-wire probe, mounting arm, and shear stress sensor.

The second large acrylic panel which contains three smaller acrylic instrumentation windows is equipped with twenty-eight 1.52-mm-diam static pressure taps spaced 2.54 cm apart along the length of the panel to measure the mean pressure along the top surface using a pneumatic pressure scanner with eight channels with an accuracy of ± 1.25 Pa. Since a zero pressure gradient is desired, an experimental parametric sweep over both tunnel velocity and the flap angle of the trailing edge (TE) is performed. For a given tunnel velocity and TE flap angle, a linear regression is found over the mean static pressure measurements and their respective locations to return a pressure gradient. Thus, for each tunnel velocity, a zero for the pressure gradient for a sweep of TE flap angles is interpolated, resulting in the zero pressure gradient TE flap angle.

The primary sensing location of the wall shear stress sensor used in this study is the center of the second acylic window, 141 cm from the leading edge. Directly downstream of the leading edge piece, a distributed roughness element is installed, a sandpaper strip of length 6.5 cm that runs the full span of the wind tunnel. The roughness height was determined using an assumed distributed roughness critical trip height Reynolds number of 120 [23], the given downstream distance of the sensor and a nominal tunnel velocity of 20 ms^{-1}, resulting in approximately a 0.6-mm distributed roughness height, to a grit size of P30, used in all experiments.

C. Capacitive shear stress sensor

A MEMS based differential CSSS system, shown in Fig. 2, developed at the University of Florida's Interdisciplinary Microsystems Group, was used in this study. The transduction of wall

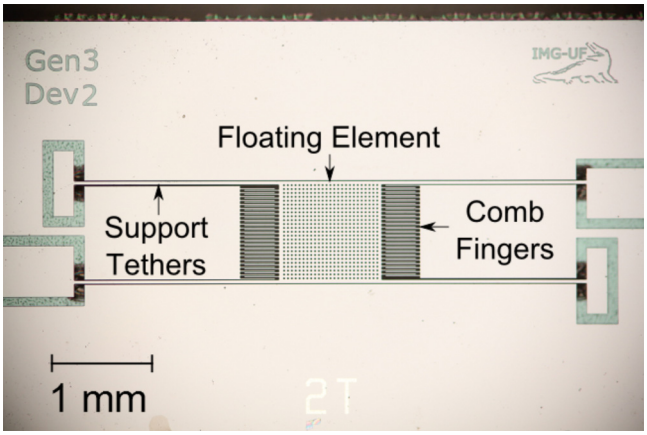

FIG. 2. Fabricated CSSS device with H-bar supporting tethers and interdigitated fingers on either side of floating element, along with hole array on the floating element for pressure rejection. (Figure was adapted from Ref. [24].)

shear stress is based on the displacements of the capacitive fingers, where a differential scheme between the sensor and the two external electrodes allows for rejection of common mode deflection [25]. The design factors critical to the study involve trade-offs between spatial resolution in terms of sensor area and sensitivity to forces, as well as between sensitivity and attenuation when fabricating either a smaller capacitive gap or including more interdigitated fingers [26]. For the current experiments, the floating element has dimensions 1×1 mm^2, corresponding to a sensor length of 51×51 squared viscous units or $0.03\delta \times 0.03\delta$ for the 20-ms^{-1} runs. The dimensions will result in spatial averaging only for the smallest structures in the flow, while still being much smaller than the scales of interest of $O(\delta)$ [27].

The MEMS manufacturing processes allow for the sensor and packaging to be hydraulically smooth, requiring height perturbations to be less than five viscous wall units to allow for viscous dissipation to suppress flow perturbations [28]. However, a wire bond required for the electronic connection of the sensor to the interface circuit, in addition to room-temperature-vulcanizing silicone sealant, has an approximate height of 200 μm, or about ten viscous wall units above the wall. This height perturbation, required for the electronics of the current packaging, was positioned away from the sensor in the spanwise direction and in the opposite direction to the spanwise traverses of the hot-wire probe to reduce impact on the measurement to avoid flow disruption directly downstream of the sensor. Future design considerations will eliminate this height perturbation using through-silicon vias for backside electronic connection.

Wall shear stress sensitivity was calculated using an acoustic plane wave tube (PWT) with the experimental setup and procedures outlined by Sheplak *et al.* [29] and Chandrasekharan *et al.* [25]. A summary of the technique is as follows: Standing wave patterns within the PWT generated by an acoustic driver on one end and a sound hard termination on the other end allow for discrete nodes of minimum pressure and maximum acoustic velocity separated by half wavelength intervals. A modified solution to Stokes's second problem allows for estimation of wall shear stress from pressure measurements at the sound hard termination of the tube. With a standing wave ratio inside the plane wave tube greater than 40 dB, locating the CSSS at a pressure node allows for measuring system response to theoretically pure wall shear stress input. In practice, the finite sensor spatial size and small location uncertainty cause minor pressure input. A sensitivity of 5.43 mV Pa^{-1} at 1.128 kHz was measured by increasing the driver amplitude; this frequency corresponds to the resonance of the PWT with fixed end wall sound hard termination. In addition, the shear stress range in the current study is within the linear response of the sensor, in both mean and dynamic component, as seen in Ref. [24]. Mounting the CSSS at the PWT termination axially aligned with

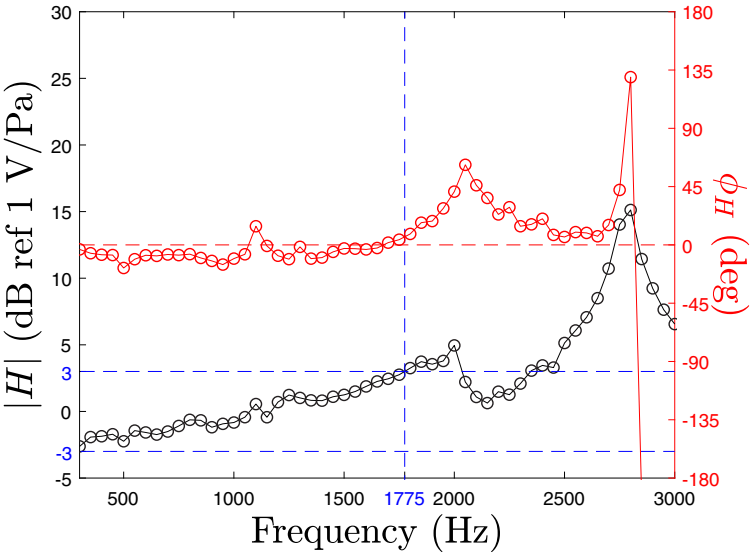

FIG. 3. Frequency response of transfer function between CSSS and streamwise aligned wall mounted microphone in PWT. Black circles (lower curve) show the magnitude response in dB showing a ±3-dB bandwidth limit of 1775 Hz. Red circles (upper curve) show the difference between the measured phase and the theoretical phase.

the flow and receiving maximum pressure and no shear stress input yields a pressure rejection ratio of 71 dB. This was achieved in part by the hole array along the element face. A high pressure rejection ratio is critical in floating element–type sensors due to the much higher pressure magnitude at the wall compared to shear stress [3].

A frequency response function is generated by using a variable position end wall termination, varying the PWT length, and thus modifying the resonant frequency while maintaining the CSSS at a pressure node for a given input frequency. Measurements are made from 300 Hz to 3 kHz, limited at the low end by the compression driver output capabilities and by sensor resonance at the high end. The frequency response between the pressure at the end wall and the CSSS is seen in Fig. 3. Sensor resonance is located at 2.8 kHz, with the usable flatband based on a ±3-dB standard extending up to 1775 Hz. The magnitude response was offset to be 0 dB at 1128 Hz, the resonance for the PWT with the fixed back plate, which has lower uncertainty than the variable position end plate. The magnitude response drops again below 3 dB before increasing above that threshold near 2.4 kHz, but the more conservative bandwidth limit at 1775 Hz was used in this study. The theoretical phase between the pressure at the end wall and wall shear stress at the first pressure node is 45°. Figure 3 shows the measured phase between the two with 45° subtracted to view differences between the theoretical and measured phases, and within the sensor bandwidth, no consistent significant difference in phase was found.

D. Hot-wire anemometry

The streamwise velocity was measured using constant temperature hot-wire anemometry (CTA), operated at an overheat ratio of 1.7. A Dantec 55P15 boundary layer–type miniature single normal probe, with a 1.25-mm sensing length and a 5-μm-diam tungsten wire is mounted in the flow on a Dantec 55H20 straight probe support. This probe support is itself attached to a mounting arm, surrounded by the NACA0012 shell, that is connected to the traversing ceiling. The scoop shape of this probe along with the mounting end that holds it allows for the sensing element to be as close to the wall as possible, without contact interference from the mounting arm. The viscous scaled probe

sensing length of 63 viscous units is larger than the empirically suggested 20 viscous units to avoid attenuation of the smallest flow scales and location of the peak of streamwise normal stress intensity, while the sensing length scaled in outer units is about 0.04δ [27]. Thus spatial attenuation due to sensing element length is expected for the small scale energy but not the large scale. However, these small scales are not the focus of these experiments, which are primarily concerned with scales of $O(\delta)$ and above.

In situ calibration was performed in the freestream of the ELD tunnel above the flat plate, far from both the flat plate turbulent boundary layer and the tunnel walls. Ten calibration points were used, ranging from 0 to 25 ms^{-1}, designed for a nominal experimental run speed of 20 ms^{-1} against the pitot-static probe of the ELD tunnel. A fifth-order polynomial was used to fit the output voltage from the CTA bridge to the tunnel velocity. This procedure was performed before and after the traverse steps were performed, and if the calibrations differed by more than 1% at the desired run speed, the experiment was repeated. The systems frequency response to a 3-kHz square wave generated by the CTA bridge was about 33 kHz [30]. All of the measurements in this study were made at sampling frequency of 10 kHz, low-pass filtered both forward and reverse in time to prevent phase distortion, using a sixth-order Butterworth filter at a cutoff of 1775 Hz for simultaneous measurement of shear stress and velocity. For each wall-normal position of the hot-wire probe, a total record of 2.5×10^5 samples of wall shear stress and velocity was taken over a record length of $T = 25$ s, or 16 490 boundary layer turnover times (TU_∞/δ). This allowed the convergence of the power spectral densities for the large scales of both wall shear stress and velocity. The unfiltered velocity signal was also recorded to analyze velocity features outside the bandwidth of the CSSS.

For all the hot-wire probe traverses in this study, the sensing element was positioned 2 mm downstream of the center of the CSSS floating element, corresponding to 101 viscous units or 0.07δ to avoid both contact and interference between the two sensors. For the traverse in the wall-normal direction, the hot-wire probe is aligned with the CSSS in the spanwise direction with logarithmically spaced points clustered near the wall in the wall-normal direction. The point closest to the wall corresponds to 28 viscous units, just inside the buffer region. For the spanwise traverse, the hot-wire probe is positioned 1.98 mm or 101 viscous units above the wall, located in the logarithmic region, with measurement positions 0.2 mm apart, or 10 viscous units. Taylor's hypothesis is used to artificially shift the streamwise location of the velocity measurement upstream to coincide with the CSSS by means of a convection velocity [31]. The frozen field hypothesis requires first low turbulence intensity with respect to the local mean $\overline{u'^2}/U^2$, which maximizes at about 0.03 for this study, and second that the wavelength of interest is smaller than δ in a boundary layer [32]. While this criterion is not strictly met, empirical studies have evaluated the validity of the frozen field hypothesis in terms of scale of interest and separation of measurement location. Recent experimental and simulation studies show that the appropriate convection velocity depends on both wave number and wall-normal position. Even so, the mean convection velocity, averaged over all wave numbers, deviates only 3.5% from the local mean streamwise velocity [33,34]. The instantaneous velocity field is well represented by the reconstructed velocity field using the mean convection velocity only up to streamwise separations of $O(\delta)$. Since the current study lacks the spatial information necessary to calculate appropriate convection velocities with regard to varying scales, the local mean streamwise velocity will be used as the convection velocity henceforth. It is expected that this pseudospectrum will alias the large scale spectral energy towards higher wave numbers [35].

III. RESULTS

Table I summarizes important boundary layer parameters calculated from mean measurements and integral analysis of both the velocity field and shear stress.

A. Wall shear stress measurements

The mean wall shear stress is captured with the CSSS, seen in Table I. Comparison of the measured c_f to the Coles-Fernholz relation $c_f = 2(\kappa^{-1}\,\mathrm{Re}_\theta + C)^{-2}$ and using the constants of

TABLE I. Boundary layer parameters.

Re_τ	Re_θ	U_∞	$\overline{\tau_w}$	c_f	U_∞^+	δ	H
1520	4420	19.9 m s^{-1}	0.692 Pa	2.87×10^{-3}	25.85	30.4 mm	1.371

Nagib *et al.* [17] results in a difference of 2.33%. The shear stress spectral density shown in Fig. 4(a) illustrates both filtered and unfiltered shear responses. The low-pass cutoff frequency corresponds to $f^+_{\text{cutoff}} \approx 0.046$ and in outer scaling, $f_{\text{cutoff}}\delta/U_\infty \approx 2.71$. Thus, only scales of $O(\delta)$ and larger are completely resolved. Clearly, bandwidth concerns for the wall shear stress sensor must be addressed for future sensors as the current flow Reynolds number cannot be substantially reduced without adversely affecting the quality of the turbulent boundary layer. The current MEMS technology does allow the LSMs and VLSMs to be resolved. Energy containing scales of smaller size are filtered, resulting in biased statistics, such as $\sqrt{\tau_x'^2}/\overline{\tau_x}$, which was observed as 0.11, highly underpredicted for the experimental Reynolds number [6]. However, this study was focused on capturing larger scales. The normalized skewness and kurtosis of the wall shear stress are 0.21 and 3.8, respectively; the corresponding probability density function (PDF) of Fig. 4(b) shows that distribution of the normalized wall shear stress is well represented by a log-normal distribution, except in the extreme tails, as are the streamwise velocity fluctuations in the viscous sublayer, shown by Alfredsson *et al.* [36]. Gomit *et al.* [37] show a much more Gaussian profile than the current work, attributed to the attenuation of the small scales. The current results indicate the existence of flow reversal events at the wall for the current Reynolds number, albeit with a very low probability. Conventional thermal sensors are unable to distinguish flow reversal events from low intensity total wall shear stress, supporting the further use of floating element sensors for higher Reynolds number flows. In other studies, these events have been shown to increase in probability with increasing Reynolds number, indicating a growth in the higher moments with Reynolds number [38], but these are extremely rare events. To ensure that the close proximity of the CSSS and hot-wire probe did not affect either measurement, the central moments up to fourth order were tracked as the probe approached the sensor, as well as the mean wall shear stress. All these statistics showed no significant deviation or trend as the hot-wire approached the CSSS, thus there was no conductive or blockage interference evident between the two sensors.

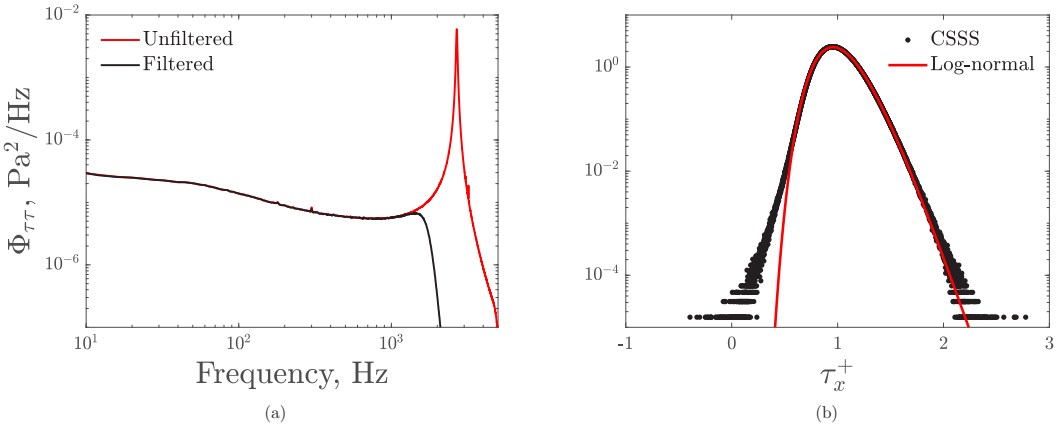

FIG. 4. (a) Unfiltered and low-pass-filtered power spectral density of τ_x', with a resonance peak at 2.8 kHz. (b) Normalized histogram simulating the PDF of measured total normalized wall shear stress, alongside a log-normal distribution matching mean and standard deviations of the data.

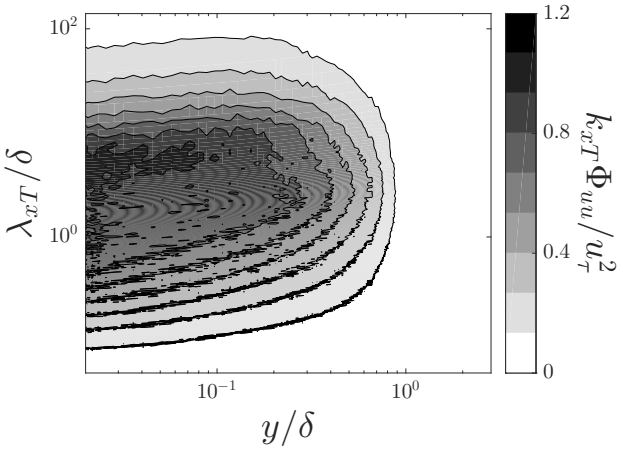

FIG. 5. Premultiplied and normalized power spectral density of unfiltered streamwise velocity for a variety of wall-normal positions.

B. Velocity measurements

Figure 5 presents the unfiltered premultiplied streamwise velocity power spectral density at various wall-normal positions. Both the wavelength λ_{xT} and wave number k_{xT} are reconstructed spatial variables from the temporal data collected here and Taylor's hypothesis using the local mean velocity as the convection velocity [33]. The spectral density decreases as distance from the wall increases, with a clear streak attributed to the large scales at a wavelength $\lambda_{xT} \approx 6\delta$.

Figure 6(a) displays the mean streamwise velocity profile normalized using the measured friction velocity from the CSSS. A comparison was made to the Schlatter-Örlü [5] zero pressure gradient turbulent boundary layer direct numerical simulation (DNS) data set for a similar but smaller $\mathrm{Re}_\theta = 4060$, with which the current data show good agreement. The slightly higher plateau reached by the current data compared to the DNS can be attributed to the difference in Reynolds number, with the current experiment having the higher Reynolds number. The difference between the CSSS friction velocity and the friction velocity extracted when fitting the velocity profile to either a

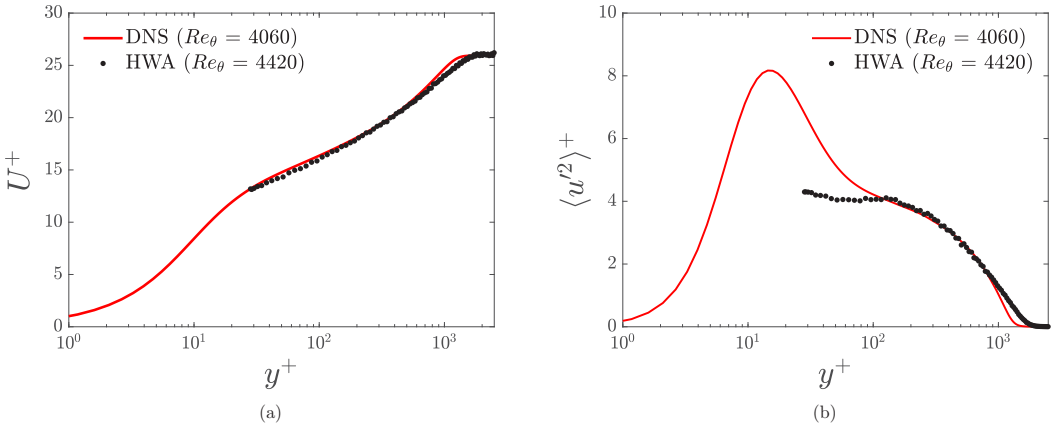

FIG. 6. (a) Mean normalized velocity profile with friction velocity extracted from CSSS and (b) normalized streamwise velocity variance, each compared to their respective profile from the Schlatter-Örlü [5] DNS data for a zero pressure gradient turbulent boundary layer at comparable Reynolds number.

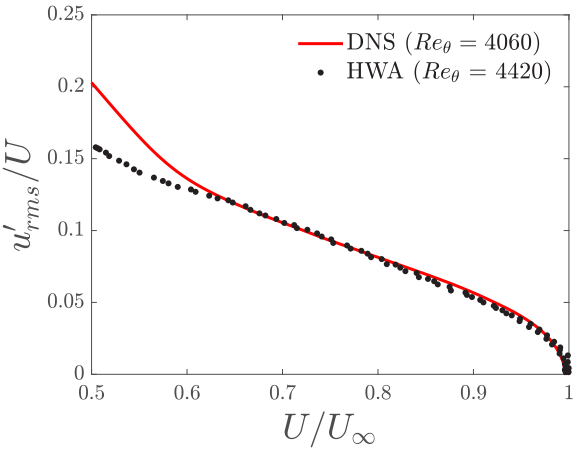

FIG. 7. Diagnostic plot formulation for the streamwise turbulence intensity compared to the Schlatter-Örlü [5] DNS data.

Spalding or Musker fit by means of least squares regression was less than 2%. The regression was run over the friction velocity u_τ and the initial probe position offset y_0 [39,40]. Approaches like these for estimating skin friction are common in experiments without direct shear stress measurements, although they assume some level of universality in the log-law constants with respect to Reynolds number, initial conditions, and flow type, and even high Reynolds number experiments show a level of uncertainty in the log-law constants [41]. A similar method reported by Kendall and Koochesfahani [42] suggests $O(1\%)$ error in the friction velocity is expected using only velocity and probe position measurements, providing a level of validation for the mean streamwise velocity for the current data. The logarithmic region also agrees well with the log-law fit using the constants of Österlund [15] of $\kappa = 0.38$ and $B = 4.1$ of the equation $U^+ = \kappa^{-1} \ln y^+ + B$, well within the uncertainty levels of these constants suggested by Marusic *et al.* [41]. The streamwise normal turbulent stress profile is shown in Fig. 6(b), where, compared to the DNS data set, evidence of the increase in fluctuation intensity near the wall was not observed. This was due to spatial averaging along the length of the hot-wire probe (in the spanwise direction) near the wall, where eddies are expected to be smaller than the hot wire [27]. Good agreement was observed in the logarithmic region, with the difference in the wake region again attributed to the Reynolds number difference, with higher intensity observed in the current experiment coinciding with higher Reynolds number.

Chauhan *et al.* [43] established criteria used as a quality check for turbulent boundary layer experiments which uses an empirical fit with respect to Reynolds number of various flow parameters. In the current study, the shape factor H and velocity scale extent U_∞^+, which is the ratio between the freestream velocity and the friction velocity, directly related to the skin friction coefficient, are used as quality check criteria. Here U_∞^+ shows a less than 1% discrepancy with its empirical fit for Re_{δ^*}, and the difference between the shape factor H and its empirical fit is less than 0.005, both of which classify the current study as representative of a canonical zero pressure gradient turbulent boundary experiment using the Chauhan *et al.* criteria. In addition, Fig. 7 shows the diagnostic plot formulation introduced by Alfredsson and Örlü [44], which is the standard deviation of the streamwise velocity fluctuations normalized by the local mean velocity plotted against the local mean velocity normalized by the freestream velocity. Normalizing the current data in this manner shows the expected linear region, independent of Reynolds number, with a slope depending on the local roughness [45]. The good fit between the data acquired in this study and the DNS in the linear region further suggests this to be a canonical flat plate turbulent boundary layer. The discrepancies in the lower speed region (i.e., closer to the wall) are further effects of spatial averaging.

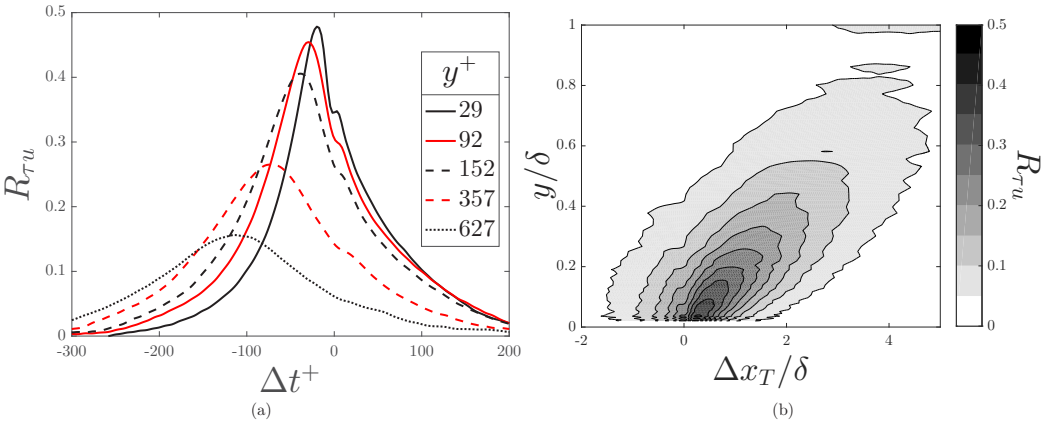

FIG. 8. For a wall-normal traverse, cross correlation coefficient $R_{\tau u}$ for (a) inner normalized temporal delays Δt^+ and (b) transformed to the spatial domain with Taylor's hypothesis.

C. Correlations and coherence

Figure 8(a) presents the temporal cross correlation between wall shear stress and streamwise velocity for select wall-normal positions. While these are captured as time series, after the artificial lag in time to compensate for the streamwise distance, Taylor's hypothesis is used to convert the signals to the spatial domain in Fig. 8(b) by imposing the local mean streamwise velocity as the convection velocity [31]. The large degree of linear correlation in Fig. 8 suggests that low-order techniques for modeling events stochastically based on correlation between the two would be successful [13]. Velocity events leading shear events in time, evident in Fig. 8(a), imply the existence of a large scale motion inclined with respect to the wall. The most common characteristic of the LSMs is the inclination angle, shown to be Reynolds number invariant near 14° [46]. This angle was calculated by using the frozen field hypothesis at each wall-normal position, with the temporal lag at the correlation peak corresponding to a streamwise distance. Significant levels of correlation persist up to the end of the logarithmic region, with two distinct qualitative features evident in Fig. 8(b). The first is the inclination of the large scale structures (note the different scales for the x and y axes) and the second is the broadness of the correlation, as opposed to a sharp peak, which diminishes the certainty by which an inclination angle can be observed. Because of these two characteristics, two peak tracking methods are used to determine the appropriate lag for calculating the inclination angle. First, the lag associated with the maximum correlation is tracked with wall-normal position. Second, the expected correlation lag, or the average lag weighted by the correlation value, in essence, the first moment of the correlation lag, is tracked at each wall-normal position. This method was proposed to track the location of the bulk correlation, which differs from the overall maximum due to the skewness in the correlations. Figure 9 shows the result, with the first peak tracking method finding an inclination angle of 15° and the second 16°. The two methods achieve similar results, with the coefficient of determination r^2 (in this simple linear regression, the square of the correlation coefficient) of the first and second peak tracking methods being 0.947 and 0.967, respectively.

The hot-wire traverse was also performed in the spanwise direction at $y^+ = 99$ with the spatial reconstruction in the streamwise direction presented in Fig. 10. The size of the correlated region in the spanwise direction is approximately 150 viscous units (0.11δ) at the wall-normal location referenced; at the same correlation threshold, the wall-normal extent is about 700 viscous units (approximately equal to 0.5δ), while the correlation extent in the streamwise direction through frozen field reconstruction is much larger than both at approximately 5 boundary layer thicknesses, seen in Fig. 8(b). These spatial extents indicate thin and long structures that reach into the wake region, qualitatively supporting the hairpin vortex packet model. In Fig. 10, at the traverse points

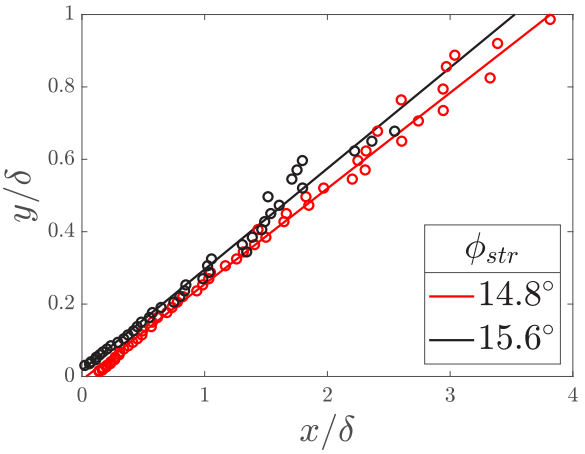

FIG. 9. Spatial reconstruction of the large scale motion for the wall-normal traverse using the chosen correlation lag value as the lag at the highest correlation peak (red circles) and the expected correlation lag from the wall-normal traverse (black circles).

farther from the shear sensor in the spanwise direction, there is evidence of a bimodal structure at this particular wall-normal location. This is supported by Ref. [47], where negatively correlated side lobes between the wall shear stress and streamwise velocity are seen farther from the sensor than the current domain of wall-normal positions.

The magnitude-squared coherence spectra is given by

$$\gamma^2_{\tau u}(y, f) = \frac{|\phi_{\tau u}(y, f)|^2}{\phi_{\tau\tau}(y, f)\phi_{uu}(y, f)}, \tag{1}$$

where $\phi_{\tau u}(y, f)$ is the one-sided cross-spectral density between the wall shear stress and velocity signals at the given wall-normal position and $\phi_{\tau\tau}(y, f)$ and $\phi_{uu}(y, f)$ are the autospectral densities of wall shear stress and velocity, respectively, for a given probe position. The high linear coherence levels support these inferred sizing of the structure, decaying rapidly after approximately 700 viscous units in the wall-normal direction in Fig. 11(a) and 150 viscous units in the spanwise

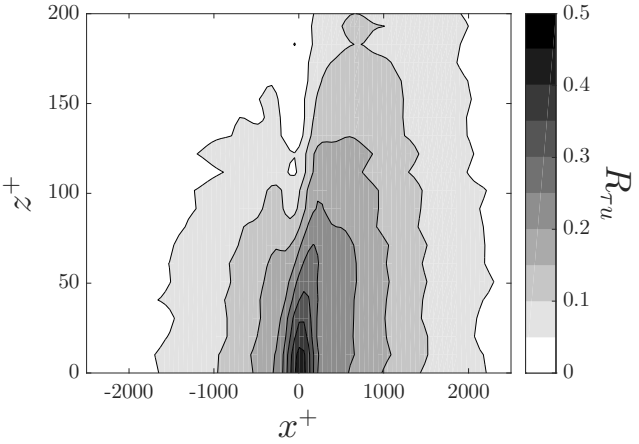

FIG. 10. For a spanwise traverse at $y^+ = 99$, the inner normalized temporal cross correlation coefficient between shear stress and streamwise velocity transformed to the spatial domain in streamwise direction.

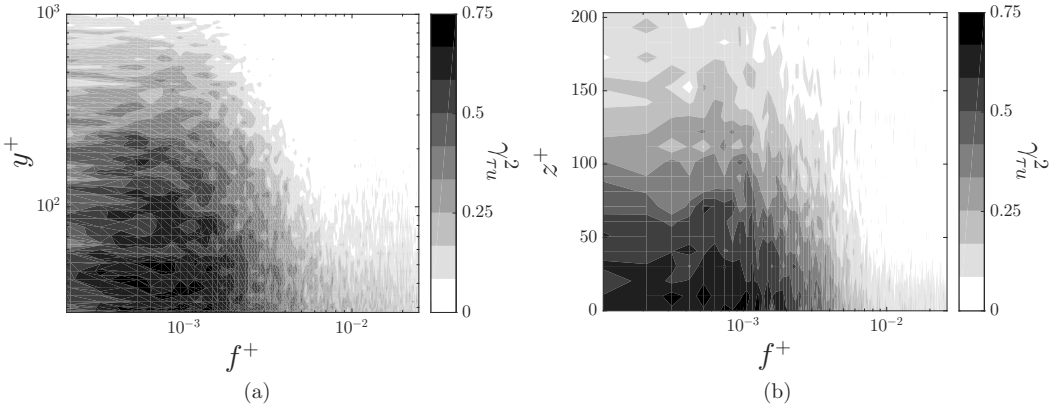

FIG. 11. Coherence between fluctuating wall shear stress and velocity signals for (a) a wall-normal traverse and (b) a spanwise traverse of the hot-wire probe at $y^+ = 99$.

direction in Fig. 11(b). However, the spatial reconstruction can only be inferred here with Taylor's hypothesis, and since there clearly exist scales larger than δ, applicability of the frozen field hypothesis is at the very least unsure. The diagnostic plot in Fig. 7 serves a secondary purpose here in also being a threshold limit for another assumption in Taylor's hypothesis, low local relative turbulence intensity u'_{rms}/U [31,32]. As u'_{rms}/U increases near the wall, it no longer becomes negligible and backflow events are possible (evident in the shear stress histogram, but not the hot-wire data due to the transduction mechanism), which severely weakens the applicability of the hypothesis. Compounding the issue, low levels of mean shear are an additional assumption. Even with its prevalence in the hot-wire experimental community, a substitute for Taylor's hypothesis must be found if ever increasing Reynolds number experiments want to use point measurements, regardless of averaging issues that have also plagued these types of measurements [27]. Therefore, at best, only qualitative statements can be made about the largest scales in this study; higher Reynolds number experiments need a true spatial measurement like particle image velocimetry, even if the noise threatens correlation values, if they hope to avoid skewing and over interpreting data.

The coherence is dominated by the lower frequencies, seen in Fig. 11(a), well into the wake region, as well as in Fig. 11(b) for the spanwise traverse. The high frequencies show low significant coherence only near the wall (less than 100), implying motions at this scale have no large impact away from the wall. Measurements closer to the wall with greater bandwidth would be required to derive higher levels of confidence on the impact the near wall small scales have relating wall shear stress and velocity, while avoiding many of the issues dealing with anemometry in the region [18].

D. Conditional measurements

The advantages of a direct time resolved measure of shear stress include the ability to conditionally sample the velocity field based on a shear stress condition. In a similar study by Hutchins *et al.* [48], only the sign of the shear stress fluctuations is used as the threshold, and in a study by Gomit *et al.* [37], the signal is divided into four equally represented quartiles for thresholding, although the measured PDF in that work is notably not skewed.

In this study, a series of thresholds are used on the local shear stress fluctuation $\tau'_x(t)$ to describe certain velocity field statistics. The resulting conditional mean velocity fields are

$$\widetilde{U}^+_{hh}(y) = \langle u(y,t) | \tau'_w(t) > \sigma_\tau \rangle, \tag{2}$$

$$\widetilde{U}^+_{h}(y) = \langle u(y,t) | \tau'_w(t) > 0 \rangle, \tag{3}$$

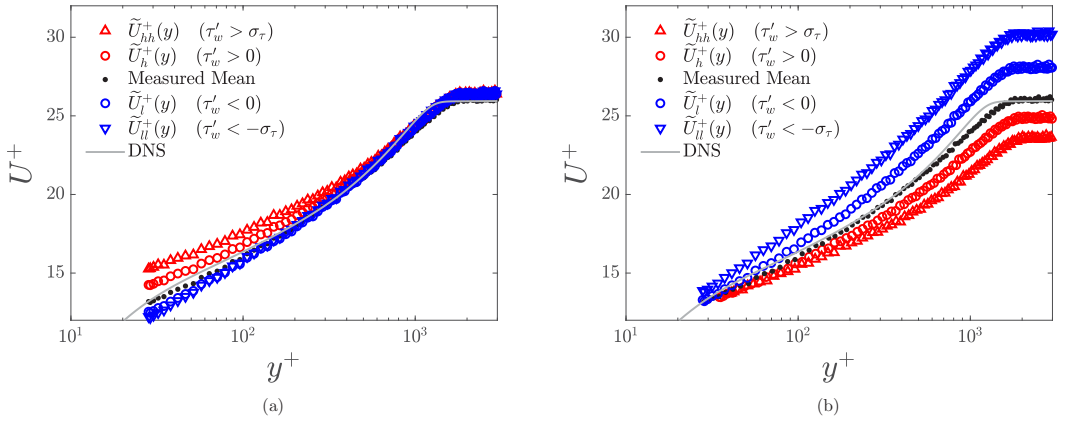

FIG. 12. Mean streamwise velocity profiles conditioned on shear events compared to the measured mean profile and DNS data from Schlatter and Örlü [5], normalized by (a) the measured total mean friction velocity and (b) the conditional mean friction velocity for each threshold.

$$\widetilde{U}^+_l(y) = \langle u(y,t) | \tau'_w(t) < 0 \rangle, \tag{4}$$

$$\widetilde{U}^+_{ll}(y) = \langle u(y,t) | \tau'_w(t) < -\sigma_\tau \rangle, \tag{5}$$

where σ_τ represents the standard deviation of the wall shear stress. These inner scaled profiles can each be normalized by the unconditional mean friction velocity u_τ, shown in Fig. 12(a), or by the conditional mean friction velocity of the respective threshold used in Eqs. (2)–(5), shown in Fig. 12(b). Qualitative agreement with the results of Hutchins *et al.* [48] is seen, and the observed trend continues for tighter thresholds; for the profile in Fig. 12(a), high shear at the wall corresponds to a steeper wall gradient, and therefore a raised velocity profile, with the trend continuing for an increased shear condition. This trend is also symmetric for low shear stress. The collapse of the mean profiles with unconditional normalization in the outer region suggests that the effect of the wall shear stress on the outer region of the mean velocity profile is minimal, at least for the current thresholds. This implies a limit to the extent conditional measurements or even flow control can have on the outer boundary layer, but a more extensive range of Reynolds number is required to find that limit and its scaling.

For a given wall-normal position, 2.5×10^5 discrete velocity samples were taken. The thresholds above and below the mean each include nominally 50% of the measurements. The thresholds above and below one standard deviation include 16% of the measurements, or about 4×10^4 samples. Increasing the threshold to study extremely intense but rare events would require more samples to be statistically converged.

The conditional velocity profiles can also be normalized with a friction velocity representative of the conditionally sampled shear stress, presented in Fig. 12(b). A profile normalized this way will follow classic universal boundary layer scaling near the wall but have modified wake regions. This shows that low shear events represent a profile with a lower friction velocity and a stronger wake, resembling an adverse pressure gradient profile. Similarly, high shear events have a higher friction velocity and reduced wake region, resembling a favorable pressure gradient. The collapse near the wall is evidence of more appropriate conditional scaling and that there is still universality in the logarithmic region and lower, with the pressure gradient–like effects only seen in the outer region. Thus, a high shear event presents the wall with an instantaneously more full boundary layer.

Of future interest is the application of these thresholds with flow reversal effects ($\tau_w < 0$) to see how a conditional mean profile is shaped under these extreme events. However, either many

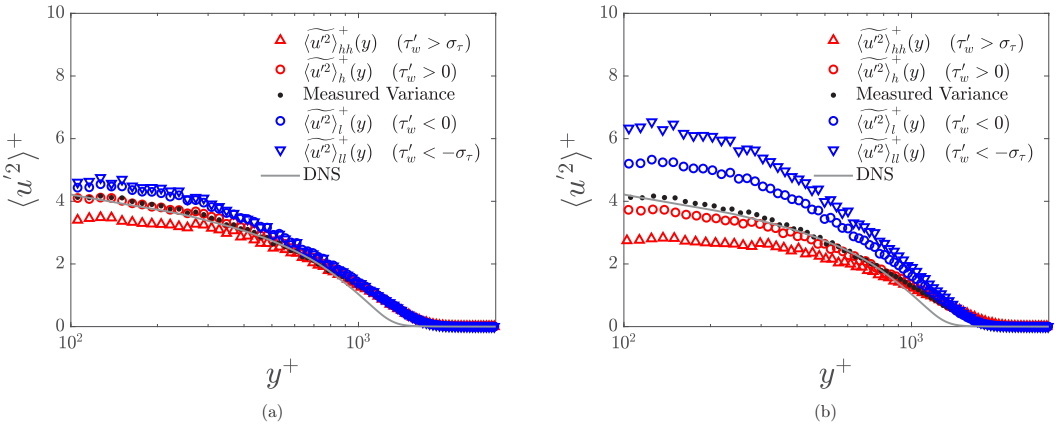

FIG. 13. Streamwise velocity variance profiles conditioned on shear events compared to the measured variance profile and DNS data from Schlatter and Örlü [5], normalized by (a) the measured total mean friction velocity and (b) the conditional mean friction velocity for each threshold.

more samples [$O(10^8)$] than the current study or a much higher Reynolds number with only weakly increasing probability of flow reversal events would be required to converge the statistics with that condition. In addition, a higher bandwidth sensor would be required to prevent temporal attenuation of these scales, so a large Reynolds number range experimental setup can begin to model this trend for future experiments.

To elucidate the effects of local shear intensity on turbulence, the thresholding procedure was performed on the streamwise normal stress profiles, as

$$\widetilde{\langle u'^2 \rangle}^+_{hh}(y) = \langle u'^2(y,t) | \tau'_w(t) > \sigma_\tau \rangle, \tag{6}$$

$$\widetilde{\langle u'^2 \rangle}^+_{h}(y) = \langle u'^2(y,t) | \tau'_w(t) > 0 \rangle, \tag{7}$$

$$\widetilde{\langle u'^2 \rangle}^+_{l}(y) = \langle u'^2(y,t) | \tau'_w(t) < 0 \rangle, \tag{8}$$

$$\widetilde{\langle u'^2 \rangle}^+_{ll}(y) = \langle u'^2(y,t) | \tau'_w(t) < -\sigma_\tau \rangle. \tag{9}$$

Higher moments of the velocity field are unable to be extracted using this procedure because of the larger sample requirement for convergence.

The conditional variance profiles are shown in Fig. 13, again in unconditional scaling shown in Fig. 13(a) and conditional mean friction velocity scaling for the respective thresholds shown in Fig. 13(b). For the unconditional normalization, only small differences between the conditional profiles and the total mean are observed. Nevertheless, negative shear fluctuation conditions result in slightly higher turbulence intensities in the logarithmic region, with high shear conditions having the opposite effect, and all the profiles collapse to zero at the boundary layer edge. The conditioning therefore seems to have the opposite effect on the variance profiles compared to the mean profiles. When applying the conditional normalization as in Fig. 13(b), these small differences are amplified. Wall-normal values near the wall are ignored here because of spatial attenuation evident in Fig. 6(b), deviating from the DNS below $y^+ = 100$, to avoid drawing incorrect conclusions about the near wall velocity field. The result of the conditional normalization in Fig. 12(b) is a collapsed mean profile near the wall, but the logarithmic region is much more energetic for low shear than normal in Fig. 13(b), and the local high shear causes a pacified logarithmic variance. This is representative of the bursting-sweeping process, but the effect of local instantaneous pressure gradients, not measured in this study, cannot be separated from this result.

IV. CONCLUSION

A MEMS based CSSS was used to measure aspects of a zero pressure gradient turbulent boundary layer at $Re_\tau = 1520$. The chosen Reynolds number balances the need to create a fully turbulent boundary layer while minimizing the effects of spatiotemporal averaging and resolving at least the LSMs. The current direct shear transduction system was shown to produce results consistent with previous wall mounted shear sensors such as hot film sensors, without the effects of frequency-dependent conduction loss, rectification, and other issues. This study demonstrated the ability of the CSSS to capture LSMs in a canonical turbulent boundary layer and their correlated relationship with the wall shear stress, as well as capturing conditional statistics of high and low shear events to differentiate their effect on the velocity field.

First, the boundary layer over the flat plate model was characterized and the data verified to be representative of a canonical zero pressure gradient turbulent boundary layer. However, the limitations of the floating element sensor include a bandwidth-limiting resonance, requiring a low-pass filter, so attenuation of different energy scales was carefully analyzed. As such, the fluctuating shear stress intensity was underpredicted for this Reynolds number. Regardless, simultaneous measurement with a single component hot-wire anemometer allowed for estimating characteristics of the LSMs through correlations, as well as conditional velocity measurements during directly measured shear events to demonstrate the sensor's ability to resolve the imprint of the turbulent structures in the boundary layer.

The measured mean wall shear stress was used to independently normalize boundary layer profiles, showing good agreement with common composite profiles, as well as a DNS data set at a similar Reynolds number [5,39]. High levels of cross correlation between the simultaneously sampled shear stress and velocity signals were reported, especially near the wall. High levels of coherence between the two signals persisted well into the wake region for the low frequencies, with almost no high frequency coherence except near the wall. Measurements in both the wall-normal and spanwise directions suggested that the LSMs are larger in the wall-normal direction than in the spanwise direction, each being much smaller than the streamwise extent.

The inclination angle of the LSMs was identified by tracking the spatial separation of the peak in the correlations, after applying the frozen field hypothesis to the temporal correlation. A peak tracking methodology was introduced that is more robust in sensing the large scale angle as opposed to small scale correlation peaks near the wall, which change the angle measurement. While a Reynolds number invariance has been shown near 14° [46], this study observed the angle at 16°. Taylor's frozen field hypothesis is the most prevalent tool to infer spatial statistics from point measurements, but its validity has been shown to break down, even at the relatively low Reynolds number of this study.

The average velocity as a function of wall-normal distance was calculated given threshold conditions of shear stress, with different normalization schemes elucidating information about different regions in the boundary layer. The conditional variance profiles, on the other hand, seem to complicate the theory that different normalization schemes can be applied to collapse the statistics of the different parts of the boundary layer. Application of the differing shear conditions, while directly modifying the local mean shear, also have a large indirect impact in conditioning on dynamic processes.

ACKNOWLEDGMENTS

This material was based upon work supported by the National Science Foundation Graduate Research Fellowship under Grant No. DGE-1315138 and the Sandia Campus Executive Fellowship PO No. 1266026. The authors also wish to acknowledge the support of the Florida Center for Advanced Aero-Propulsion and the National Science Foundation under Grant No. CBET-1744146.

[1] K. G. Winter, An outline of the techniques available for the measurement of skin friction in turbulent boundary layers, Prog. Aerosp. Sci. **18**, 1 (1977).
[2] J. H. Haritonidis, in *Advances in Fluid Mechanics Measurements*, edited by M. Gad-El-Hak (Springer, Berlin, 1989), pp. 229–261.
[3] J. W. Naughton and M. Sheplak, Modern developments in shear-stress measurement, Prog. Aerosp. Sci. **38**, 515 (2002).
[4] A. Wietrzak and R. M. Lueptow, Wall shear stress and velocity in a turbulent axisymmetric boundary layer, J. Fluid Mech. **259**, 191 (1994).
[5] P. Schlatter and R. Örlü, Assessment of direct numerical simulation data of turbulent boundary layers, J. Fluid Mech. **659**, 116 (2010).
[6] P. H. Alfredsson, A. V. Johansson, J. H. Haritonidis, and H. Eckelmann, The fluctuating wall-shear stress and the velocity field in the viscous sublayer, Phys. Fluids **31**, 1026 (1988).
[7] C. Brücker, J. Spatz, and W. Schröder, Feasability study of wall shear stress imaging using microstructured surfaces with flexible micropillars, Exp. Fluids **39**, 464 (2005).
[8] S. Große and W. Schröder, High Reynolds number turbulent wind tunnel boundary layer wall-shear stress sensor, J. Turbul. **10**, N14 (2009).
[9] O. Amili and J. Soria, A film-based wall shear stress sensor for wall-bounded turbulent flows, Exp. Fluids **51**, 137 (2011).
[10] S. Robinson, Coherent motions in the turbulent boundary layer, Annu. Rev. Fluid Mech. **23**, 601 (1991).
[11] R. J. Adrian, Hairpin vortex organization in wall turbulence, Phys. Fluids **19**, 041301 (2007).
[12] G. L. Brown and A. S. W. Thomas, Large structure in a turbulent boundary layer, Phys. Fluids **20**, S243 (1977).
[13] R. Mathis, I. Marusic, S. I. Chernyshenko, and N. Hutchins, Estimating wall-shear-stress fluctuations given an outer region input, J. Fluid Mech. **715**, 163 (2013).
[14] H. H. Fernholz and P. J. Finley, The incompressible zero-pressure gradient turbulent boundary layer: An assessment of the data, Prog. Aerosp. Sci. **32**, 245 (1996).
[15] J. M. Österlund, Experimental studies of zero pressure-gradient turbulent boundary-layer flow, Ph.D. thesis, Royal Institute of Technology, 1999.
[16] H. M. Nagib and K. A. Chauhan, Variations of von Kármán coefficient in canonical flows, Phys. Fluids **20**, 101518 (2008).
[17] H. M. Nagib, K. A. Chauhan, and P. A. Monkewitz, Approach to an asymptotic state for zero pressure gradient turbulent boundary layers, Philos. Trans. R. Soc. A **365**, 755 (2007).
[18] I. Marusic, B. J. McKeon, P. A. Monkewitz, H. M. Nagib, A. J. Smits, and K. R. Sreenivasan, Wall-bounded turbulent flows at high Reynolds numbers: Recent advances and key issues, Phys. Fluids **22**, 065103 (2010).
[19] M. Guala, M. Metzger, and B. J. McKeon, Interactions within the turbulent boundary layer at high Reynolds number, J. Fluid Mech. **666**, 573 (2011).
[20] M. Vallikivi, B. Ganapathisubramani, and A. J. Smits, Spectral scaling in boundary layers and pipes at very high Reynolds numbers, J. Fluid Mech. **771**, 303 (2015).
[21] S. Pirozzoli and M. Bernardini, Probing high-Reynolds-number effects in numerical boundary layers, Phys. Fluids **25**, 021704 (2013).
[22] R. E. Hanson, H. P. Buckley, and P. Lavoie, Aerodynamic optimization of the flat-plate leading edge for experimental studies of laminar and transitional boundary layers, Exp. Fluids **53**, 863 (2012).
[23] H. Schlichting, *Boundary Layer Theory*, 4th ed. (McGraw-Hill, New York, 1960).
[24] C. Barnard, J. Meloy, and M. Sheplak, *Proceedings of 2016 IEEE Sensors, Orlando* (IEEE, Piscataway, 2016).
[25] V. Chandrasekharan, J. Sells, J. C. Meloy, D. P. Arnold, and M. Sheplak, A microscale differential capacitive direct wall-shear-stress sensor, J. Microelectromech. Syst. **20**, 622 (2011).
[26] J. C. Meloy, J. Griffin, J. Sells, V. Chandrasekharan, L. N. Cattafesta, and M. Sheplak, *Proceedings of the 41st AIAA Fluid Dynamics Conference, Honolulu, 2011* (AIAA, Reston, 2011), pp. 1–18.

[27] N. Hutchins, T. B. Nickels, I. Marusic, and M. S. Chong, Hot-wire spatial resolution issues in wall-bounded turbulence, J. Fluid Mech. **635**, 103 (2009).
[28] S. B. Pope, *Turbulent Flows* (Cambridge University Press, Cambridge, 2000).
[29] M. Sheplak, A. Padmanabhan, M. A. Schmidt, and K. S. Breuer, Dynamic calibration of a shear-stress sensor using stokes-layer excitation, AIAA J. **39**, 819 (2001).
[30] H. H. Bruun, *Hot-Wire Anemometry: Principles and Signal Analysis* (Oxford University Press, Oxford, 1995).
[31] G. I. Taylor, The spectrum of turbulence, Proc. R. Soc. London Ser. A **164**, 476 (1938).
[32] C. C. Lin, On Taylor's hypothesis and the acceleration terms in the Navier-Stokes equations, Q. Appl. Math. **10**, 295 (1953).
[33] C. Atkinson, N. A. Buchmann, and J. Soria, An experimental investigation of turbulent convection velocities in a turbulent boundary layer, Flow Turbul. Combust. **94**, 79 (2014).
[34] J. C. Del Álamo and J. Jiménez, Estimation of turbulent convection velocities and corrections to Taylor's approximation, J. Fluid Mech. **640**, 5 (2009).
[35] B. J. Rosenberg, M. Hultmark, M. Vallikivi, S. C. C. Bailey, and A. J. Smits, Turbulence spectra in smooth- and rough-wall pipe flow at extreme Reynolds numbers, J. Fluid Mech. **731**, 46 (2013).
[36] P. H. Alfredsson, R. Örlü, and P. Schlatter, The viscous sublayer revisited-exploiting self-similarity to determine the wall position and friction velocity, Exp. Fluids **51**, 271 (2011).
[37] G. Gomit, R. de Kat, and B. Ganapathisubramani, Structure of high and low shear-stress events in a turbulent boundary layer, Phys. Rev. Fluids **3**, 014609 (2018).
[38] C. Diaz-Daniel, S. Laizet, and J. C. Vassilicos, Wall shear stress fluctuations: Mixed scaling and their effects on velocity fluctuations in a turbulent boundary layer, Phys. Fluids **29**, 055102 (2017).
[39] D. B. Spalding, A single formula for the "Law of the wall", J. Appl. Mech. **28**, 455 (1961).
[40] A. J. Musker, Explicit expression for the smooth wall velocity distribution in a turbulent boundary layer, AIAA J. **17**, 655 (1979).
[41] I. Marusic, J. P. Monty, M. Hultmark, and A. J. Smits, On the logarithmic region in wall turbulence, J. Fluid Mech. **716**, R3 (2013).
[42] A. Kendall and M. M. Koochesfahani, A method for estimating wall friction in turbulent wall-bounded flows, Exp. Fluids **44**, 773 (2008).
[43] K. A. Chauhan, P. A. Monkewitz, and H. M. Nagib, Criteria for assessing experiments in zero pressure gradient boundary layers, Fluid Dyn. Res. **41**, 021404 (2009).
[44] P. H. Alfredsson and R. Örlü, The diagnostic plot a litmus test for wall bounded turbulence data, Eur. J. Mech. B **29**, 403 (2010).
[45] I. P. Castro, A. Segalini, and P. H. Alfredsson, Outer-layer turbulence intensities in smooth- and rough-wall boundary layers, J. Fluid Mech. **727**, 119 (2013).
[46] I. Marusic and W. D. C. Heuer, Reynolds Number Invariance of the Structure Inclination Angle in Wall Turbulence, Phys. Rev. Lett. **99**, 114504 (2007).
[47] J. A. Sillero, J. Jiménez, and R. D. Moser, Two-point statistics for turbulent boundary layers and channels at Reynolds numbers up to $\delta^+ \approx 2000$, Phys. Fluids **26**, 105109 (2014).
[48] N. Hutchins, J. P. Monty, B. Ganapathisubramani, H. C.-H. Ng, and I. Marusic, Three-dimensional conditional structure of a high-Reynolds-number turbulent boundary layer, J. Fluid Mech. **673**, 255 (2011).